Multiscale Operando X-ray Investigations Provide Insights into Electro-Chemo-Mechanical Behavior of Lithium Intercalation Cathodes

Laisuo Su[1], Paul Choi[1], Nathan Nakamura[1], Harry Charalambous[2], Shawn Litster[1], Jan Ilavsky[2], B. Reeja-Jayan[1,]*

[1] Department of Mechanical Engineering, Carnegie Mellon University, 5000 Forbes Avenue, PA, 15213, USA

[2] X-ray Science Division, Argonne National Laboratory, 9700 S. Cass Avenue, Argonne, IL, 60439, USA

Abstract

The electrochemical performance and cycle life of lithium-ion batteries (LIBs) depend on the electrochemical, chemical, and mechanical behavior of electrodes and electrolytes. Despite extensive studies conducted previously, challenges exist to decouple these behaviors, capture the evolution of electro-chemo-mechanical behavior in realistic conditions, and correlate atomic-scale stress evolution to micro-scale bulk mechanical degradation. Here, we report multiscale operando techniques to investigate polydisperse battery electrodes by integrating volume-averaged quantitative synchrotron X-ray scattering with high-resolution transmission X-ray microscopy (TXM). The former provides us information spanning a wide spatial range, from Angstrom-level atomic structures to micrometer-level particle scales, while the latter provides time-resolved 2D images of the particles during cycling. The complementarity of the two operando techniques is demonstrated by an over-lithiation test of $LiCoO_2$ electrodes, where particles crack and eventually

pulverize. Additionally, the techniques are applied to study $LiCoO_2$ cycling stability from 3.0 V – 4.5 V. Operando X-ray scattering result shows nanometer-scale features keep forming in $LiCoO_2$ electrodes during cycling, resulting in an increased projected area observed by the TXM experiment. The formation of such features is inhibited by a polymer coating on the electrode, leading to vastly improved cycling stability. The polymer coating alleviates $LiCoO_2$ surface deterioration, reduces side product generation, and inhibits $LiCoO_2$ particles volume expansion during the cycling test. These operando multimodal X-ray techniques presented herein thus offer a novel, multiscale diagnostic modality for studying existing and emerging battery materials, aiding the development of next-generation LIBs.

Keywords: Lithium-ion battery; X-ray scattering; Transmission X-ray microscopy; Operando measurement; Electro-chemo-mechanical behavior; Surface engineering

Highlights

- Operando techniques are developed to study $LiCoO_2$ electro-chemo-mechanical behavior.
- $LiCoO_2$ particles crack and eventually pulverize when discharged from 3.0 V - 0.5 V.
- Nanoscale features form in $LiCoO_2$ electrodes when cycled from 3.0 V – 4.5 V.
- A PEDOT coating improves $LiCoO_2$ cycling stability by inhibiting feature formation.

Introduction

A lithium-ion battery (LIB) is generally composed of two electrodes, a cathode, and an anode, leading to a "rocking chair battery" in which lithium ions can move back and forth [1]. Mechanical degradation has been recognized as a significant contributor to the failure of LIBs [2-6]. This is because the insertion and extraction of Li from an electrode are accompanied by volume changes

resulting from lattice parameter variations and new crystalline and amorphous phases [5,7]. For example, the volume of $LiCoO_2$ unit cell shows around 3.8% expansion during cycling [8]. The volume change leads to deformations and stress generation in the cathode, which can inversely modulate the thermodynamics and kinetics of phase evolution, charge transfer, and chemical potential of active materials in the electrodes. Additionally, the deformation may result in fragmentation, disintegration, fracturing, loss of contact between current collectors and the active electrode materials, and expose new electrode surfaces to the electrolyte, accelerating the process of capacity loss [9]. Therefore, understanding the role of electrochemical and chemical reactions on mechanical degradation is a critical precursor to tailoring the electro-chemo-mechanical behavior of next-generation LIBs.

Electro-chemo-mechanical interactions at battery electrodes can be regulated by surface engineering techniques, enhancing the electrochemical performance of LIBs [5]. The most widely adopted coatings for both cathode and anode materials are carbon [10], conductive polymers [11], metal oxides [12], metal fluorides [13], and Li^+ conductors [14], These coatings create an effective stress field and chemical potential barrier for Li^+ diffusion at the electrode surface, resulting in distinct lithiation behavior and improved rate capability compared to the pristine electrode [15]. Additionally, the coatings alleviate mechanical fatigue in the electrodes by altering their surface deterioration and electrolyte decomposition [16]. However, most of the current studies on these effects are based on ex-situ experiments that fail to capture the dynamics of mechanical changes occurring during cycling, limiting our ability to design superior surface engineering methods for battery electrodes. Thus, operando experimental techniques are needed to provide a more comprehensive guide for diagnosing and engineering current and prospective LIB materials.

A few operando techniques have been applied to investigate the mechanical degradation of battery electrodes, including acoustic emission (AE) [17], atomic force microscope (AFM) [18], scanning electron microscopy (SEM) [19], and transmission electron microscopy (TEM) [20, 21]. Operando AE technique can quantify the evolution and scale of micro-cracking in an electrode during cycling. However, it cannot directly relate the observed behavior to effects at the single-particle scale [17]. Operando AFM and SEM provide microscopic images for electrode particles at high resolution. However, these techniques are surface sensitive and cannot probe into the bulk for practical porous battery electrodes [18, 19]. Bulk characterization can be performed by applying operando TEM, but this technique offers only local information in a small probe area [20, 21]. It is also unclear how to correlate atomic nano- and micro-scale mechanical degradation to bulk structure evolution with these techniques. Additionally, it is challenging to measure the electro-chemo-mechanical behavior of electrodes under realistic conditions quantitatively because most existing operando studies characterize mechanical behavior using particular types of batteries, such as capillary cells, that may not represent realistic battery applications [20, 21].

Operando X-ray scattering and transmission X-ray microscopy (TXM) are two powerful techniques to investigate the mechanical behavior of battery electrodes during cycling. Christopher et al. provided a complete picture of the Li repartition during prelithiation and cycling of a silicon/graphite composite anode and the C-rate-dependent sequential (de)lithiation mechanisms of a Si/$FeSi_2$/graphite anode via operando small-angle X-ray scattering (SAXS) and wide-angle X-ray scattering (WAXS) [22,23]. In addition, TXM offers straightforward radiography images for understanding the electrode architecture during cycling [24]. $LiCoO_2$ possesses the highest theoretic capacity density (274 mA h/g) and packing density among commercially available

cathode materials [25, 26]. Understanding the mechanical behavior of $LiCoO_2$ is crucial to the development of LIBs [27-29].

This study combines operando X-ray scattering and operando TXM techniques to understand the mechanical behavior of $LiCoO_2$ during cycling (Figure 1). The ultra-small angle X-ray scattering (USAXS), SAXS, and WAXS provide a wide spatial range (from Angstrom scale of atomic structures to micrometer scale of bulk particles, Figure 1f) [30, 31]. TXM provides 2D radiography images that visualize the temporal evolution of individual $LiCoO_2$ particles in the standard coin cell format [32]. With the help of the two techniques, we observe the volume expansion of $LiCoO_2$ particles during cycling. Moreover, we uncover the effect of a poly(3,4-ethylenedioxythiophene) (PEDOT) artificial coating on the electro-chemo-mechanical behavior of $LiCoO_2$ during cycling. The results suggest that the PEDOT coating not only inhibits the formation of new features in $LiCoO_2$ electrodes but also alleviates $LiCoO_2$ particle expansion during long-term cycling. This work demonstrates how the X-ray scattering technique can be integrated with TXM to provide a novel operando diagnostic toolbox for investigating polydisperse systems like electrode materials in LIBs.

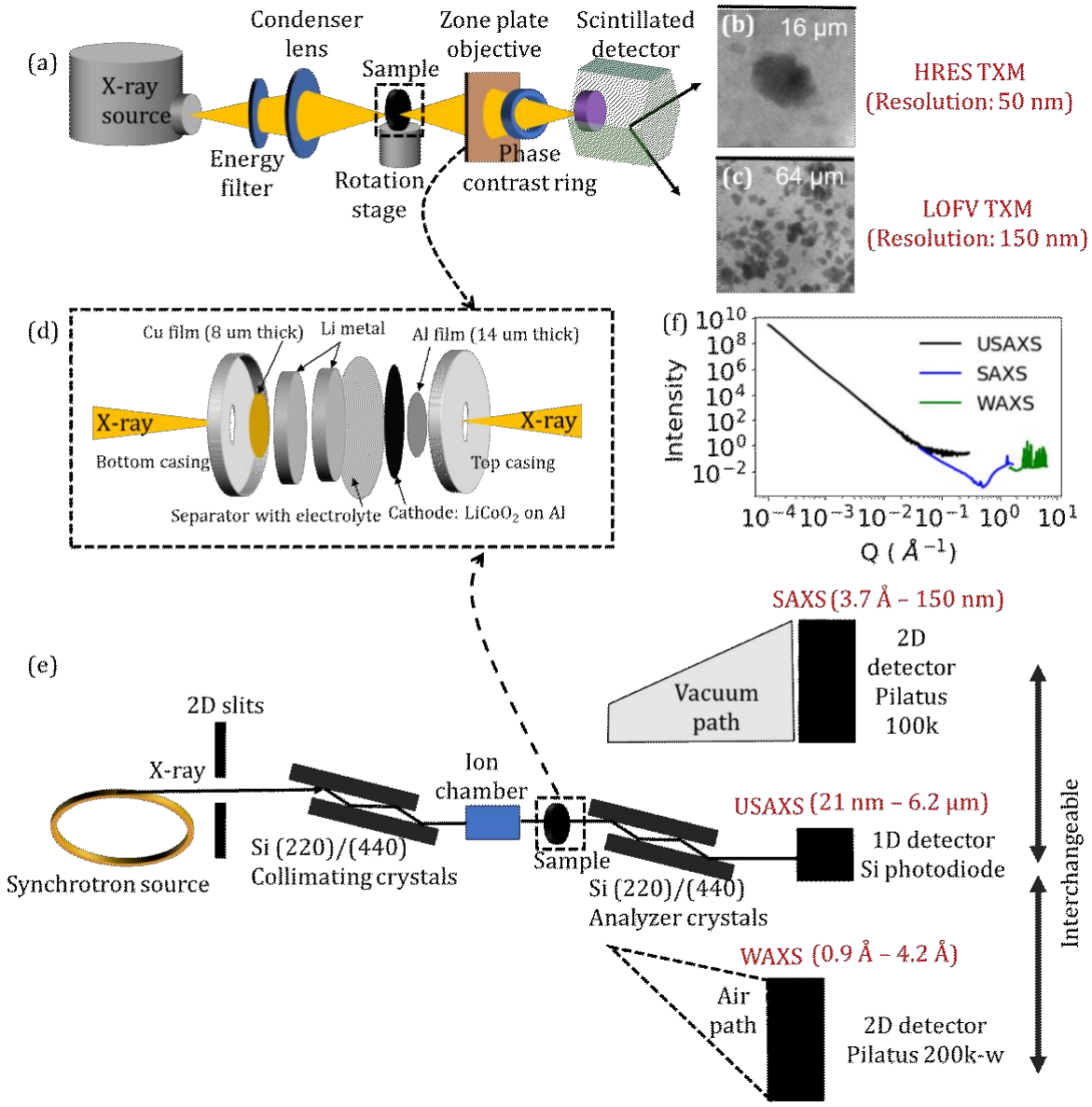

Figure 1. The experimental setups for operando studies using window coin cells. (a) A schematic of the transmission x-ray microscopy (TXM) technique using a laboratory-based 8 keV rotating copper anode X-ray source. The highest spatial resolution reaches 50 nm. Two modes are applied, including a high resolution (HRES) and a large field of view (LFOV) mode. (b, c) TXM images of a $LiCoO_2$ electrode taken using the HRES mode (b), and the LFOV mode (c). (d) A schematic of a CR-2016 type window coin cell. Al foil and Cu foil are used to seal the cathode and anode side windows, respectively. (e) A schematic of the synchrotron-based X-ray scattering technique. The three detectors (USAXS, SAXS, and WAXS) are interchangeable during the measurement. The numbers in brackets stand for the spatial range of each detector. (f) An illustration of data collected for a $LiCoO_2$ electrode using the combination of USAXS, SAXS, and WAXS detectors that covers five decades of Q-range (from 10^{-4}/Å to 6.6/Å). The large Q range suggests that the technique can detect features with a size range of 6.2 μm to 0.9 Å.

Experimentation and methods

Standard CR-2016 type coin cell casings (MTI Corporation) were modified by cutting a 3 mm diameter hole through the faces to prevent the X-ray beam's attenuation by stainless steel casings in time-resolved studies. The holes were hermetically sealed with Al and Cu foils on the cathode and anode sides, respectively, using a 1:1 weight ratio of Eccobond 45 and Catalyst 15 (GracoRoberts). A schematic of the window coin cell is shown in Figure 1d. Compared to the conventionally used insulating Kapton film for sealing, the electronically conductive Al and Cu film can reduce the inhomogeneity of the electrochemical process at the window area. Thus, the modifications had negligible effects on the overall electrochemical performance of the tested electrodes, as indicated in Fig. S1.

2320 type Celgard separators, commercial electrolytes, $LiCoO_2$ powder, and lithium metal discs were purchased from MTI Corporation. The primary particle size of $LiCoO_2$ is 2.1 μm (mean) and 1.7 μm (median) in diameter [29]. 80 % $LiCoO_2$, 10 % polyvinylidene fluoride binder, and 10 % super-P conductive agent were mixed in N-Methyl-2-pyrrolidone (NMP). The slurry was then cast onto Al current collectors. After drying in a 110 ^oC vacuum oven for 12 hours, disks with a diameter of 14 mm were punched and used as cathodes. The active material loading was around 1 mg/cm^2 to eliminate overlapping between particles during the TXM experiment. Coin cells were assembled in a glove box (Thermo Fisher Scientific) with H_2O and O_2 levels below 0.5 ppm. The components inside a coin cell are shown in Figure 1d. Two discs of Li metal (0.5 mm thick) were used as the anode to provide sufficient pressure to maintain good contact between the Li metal anode and the $LiCoO_2$ electrode. Around 100 μl of 1M $LiFP_6$ dissolved in ethylene carbonate/diethyl carbonate (1: 1 in volume) was used as the electrolyte. To study the PEDOT coating effect on the behavior of $LiCoO_2$, we engineered a 50 nm thick polymer coating on $LiCoO_2$

electrodes using a chemical vapor deposition polymerization technique, as detailed in previous publications [11, 33].

Electrochemical tests were conducted using three battery cyclers. A LAND battery cycler (LAND Electronics Co., Ltd) was used for the pre-conditioning tests, a VMP3 (Biologic Company) was used for the operando TXM experiment, and a MACCOR 4300 battery cycler (MACCOR, Inc.) was used for the operando X-ray scattering experiment. Two different protocols were investigated in this study. (1) An over-lithiation of the $LiCoO_2$ cathode, during which cells were discharged to 0.5 V at C/2 (1C = 145 mA/g) using a constant-current (CC) protocol. Of note, the cells did not undergo any pre-conditioning steps. (2) High-voltage, high-rate cycling of pre-conditioned cells, wherein the cells were pre-conditioned with a cycle at C/10 between 3.0 V – 4.2 V at room temperature (20 ^{o}C) using a LAND battery cycler. Then, the cells were cycled between 3.0 V – 4.5 V using a CC protocol. The cycling rate was set to 10 C in the operando TXM experiment and was 5C in the operando X-ray scattering experiment for both charge and discharge.

SEM was conducted on Quanta 600 (Thermo Fisher Scientific) using 10.0 kV accelerating voltages. The spot size was around 10 nm. High-resolution TXM characterization was conducted using a laboratory-scale instrument (UltraXRM-L200, Zeiss, USA) with an 8 keV rotating copper anode X-ray source (Figure 1a). Both high resolution (HRES, Figure 1b) and large field of view (LFOV, Figure 1c) data were collected in the absorption contrast mode. The HRES achieved a 50 nm resolution with a 16 μm FOV, while the LFOV mode achieved a 150 nm resolution with a 65 μm FOV. The HRES data was collected with 240 s of beam exposure and pixel binning of 1, while the LFOV data was collected with 60 s of beam exposure and pixel binning of 1. The exposure time was chosen to allow for an optimum balance of the signal-to-noise ratio and temporal

resolution of the operando datasets. As part of the analysis, a 3-by-3 LFOV mosaic image (195 μm × 195 μm) was collected first to check the distribution of $LiCoO_2$ particles. Afterward, a small area was selected for HRES imaging. Coin cells were cycled based on the two specified protocols using a VMP3 potentiostat. At the end of each experiment, an additional 3-by-3 LFOV mosaic image was collected for comparison with the initial mosaic image. A background image for X-ray image normalization was acquired and applied to enhance the contrast and the signal-to-noise ratio. Image alignment and processing were performed using ImageJ software. To quantitatively analyze the projected area of $LiCoO_2$ particles, we applied a non-local means filter, which was optimized for each of the HRES operando and LFOV MOSAIC radiographs. The filter proved to be useful at reducing overall noise and enhancing the contrast between the background and the particles of interest [34]. Also, a gaussian bandpass filter was generated and applied in Fourier space to enhance the contrast of the radiographs further and suppress any imaging artifacts that may have occurred during radiograph acquisition. An adaptive thresholding algorithm was used to generate a binary image. The segmented and binarized images of the radiographs were used to calculate the projected area of the particles.

Synchrotron X-ray scattering experiments were conducted at sector 9 ID-C at the Advanced Photon Source (APS), Argonne National Laboratory [30, 31]. The hutch was equipped with three detectors to successively measure USAXS, SAXS, and WAXS simultaneously in quick succession (Figure 1e, Fig. S2). Window coin cells were placed in a custom-designed cell holder and connected to a MACCOR 4300 battery cycler. A collimated monochromatic X-ray beam in the standard 1-D collimated transmission geometry was used to measure the scattering intensity as a function of scattering vector (Q). The beam energy was 21 keV, and the flux was ~10^{13} photon/s. The beam size was 0.8 mm by 0.8 mm. The combination of USAXS + SAXS + WAXS achieved

a five-decades combined Q-range in scatter sizes from 10^{-4} /Å to 6.6 /Å, corresponding to a coverage of length scale measurements ranging from 6.2 μm to 0.9 Å. The data acquisition time was set to 120 s, 20 s, and 20 s for the USAXS, SAXS, and WAXS measurements. The total data collection time was 216 s between each scan, considering the time spent on periodic recalibration and switching detectors.

Results and Discussion

Operando X-ray Scattering Technique to Study $LiCoO_2$ Over-Lithiation

To the best of our knowledge, no research paper has been published to investigate polydisperse battery materials using the USAXS technique. Demonstrating the feasibility of the technique is thus essential. Here, we applied the technique to investigate the over-lithiation of $LiCoO_2$ electrodes, during which they show significant morphology changes [27]. Local over-lithiation of the cathode can happen during fast discharging, which leads to heterogenous lithiation of the cathode. Also, poor battery management and when $LiCoO_2$ is utilized as a negative electrode conversion material can result in over-lithiation of $LiCoO_2$.

Thermodynamically stable Li-rich $LiCoO_2$ phases do not exist from ab initio calculations [27, 35]. Stoichiometric $LiCoO_2$ could coexist with Co metal, Li_2O, and Li_2O_2 depending on the oxygen chemical potential [27]. The over-lithiation of $LiCoO_2$ can be summarized in equation (1) and (2) [35].

$$LiCoO_2 + (x + 2y)Li^+ + (x + 2y)e^- \rightarrow Li_{1+x}CoO_{2-y} + yLi_2O \quad (1)$$

$$Li_{1+x}CoO_{2-y} + (3 - x - 2y)Li^+ + (3 - x - 2y)e^- \rightarrow (2 - y)Li_2O + Co \quad (2)$$

Figure 2 shows the operando X-ray scattering result of a $LiCoO_2$ electrode during an over-lithiation test from 3.0 V – 0.5 V at C/2. Figure 2a displays the discharge curve, which shows a plateau at around 1.0 V and matched well with existing studies [35]. Synchrotron X-ray scattering information was continuously collected during the discharge process, and five locations (1, 11, 21, 31, 41) were selected for comparison to investigate the evolution of the $LiCoO_2$ electrode at these points. Figure 2b compares the tested USAXS and SAXS data at five locations indicated in Figure 2a. A broad peak at around 0.4/Å showed up and grew during the over-lithiation test. The X-ray scattering intensity decreases linearly with Q^{-4}, as indicated in the figure. However, the evolution of the X-ray intensity at the low Q region (from 10^{-4}/Å to10^{-2}/Å) was not apparent because a log-scale was applied for the intensity value.

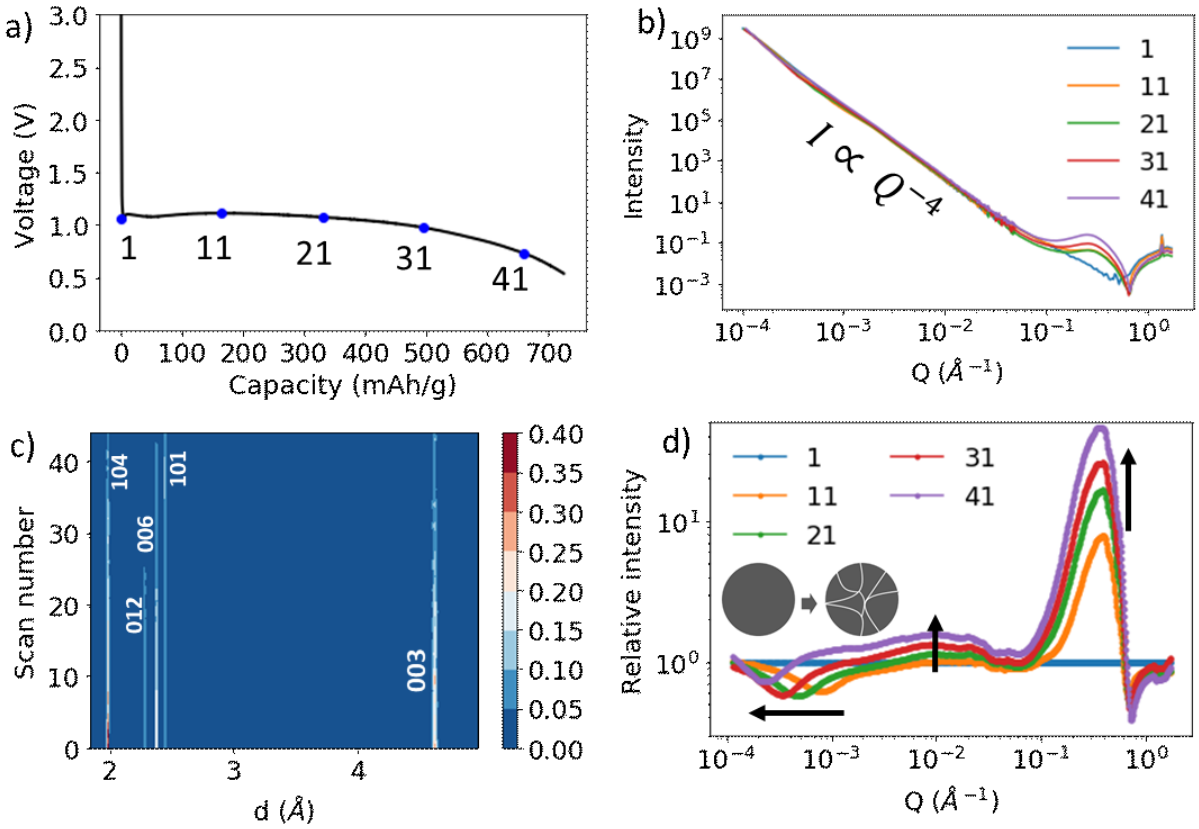

Figure 2. Operando synchrotron X-ray scattering techniques to study pristine $LiCoO_2$ electrode during an over-lithiation test. (a) Discharge curve during the over-lithiation process from 3.0 V – 0.5 V at C/2 rate. Five points are selected for the comparison of

the scattering data. (b) Selected USAXS + SAXS data at the five different points. (c) A contour plot shows the evolution of selected WAXS data to display the evolution of $LiCoO_2$ crystal peaks during the over-lithiation test. (d)) The evolution of the relative intensity (RI) of USAXS + SAXS data referred to the first scan. The inserted schematic shows the mechanism that causes the evolution of the RI value in the low Q region. The black arrows indicate the evolution of the RI curve during the test.

To better understand the X-ray scattering data, equation (3) relates the X-ray scattering intensity (I) with the scattering vector (Q) [36].

$$I(Q) = \sum_{n=1}^{N} V_n^2(Q) + 2\sum_{m<n}^{N} V_m(Q) \cdot V_n(Q)\cos(\varphi_m - \varphi_n) \quad (3)$$

Where $I(Q)$ is the intensity of the x-ray with the scattering vector Q, $V_n(Q)$ is a reflection amplitude from the n^{th} interface, and its amplitude $V \cong \left({}^{Q_c}/_{2Q}\right)^2$ with Q_c being the critical angle of the interface proportional to the electron-density jump at the interface. $\varphi_m - \varphi_n = Qd$ is the phase difference associated with the distance between the layers.

The first term represents the sum of scattering intensities from individual interfaces, and the second term represents the intensities from interference between them. When the particle size is random, the oscillatory (second) terms are averaged and canceled out. The overall scattering follows Porod's law, which states that the scattering intensity decreases linearly with Q^{-4}.

The experimental data in Figure 2b follows Porod's law in the low Q region (10^{-4}/Å to 10^{-2}/Å), suggesting that the $LiCoO_2$ electrode was a polydisperse system with approximately spherical particles comprising an extensive size range [37]. Additionally, the relationship between scattering vector Q and physical dimension d is shown in equation (4). The broad peak at around 0.4/Å corresponded to features with approximately 1.5 nm size, indicating the growth of features with a 1.5 nm length scale during the over-lithiation process.

$$d = {}^{2\pi}/_{Q} \quad (4)$$

The USAXS and SAXS data covered a Q-range (scattering vector) from 10^{-4}/Å to 1.7/Å, and the WAXS data covered a Q-range from 1.5/Å to 6.6/Å. Equation (4) suggests that the USAXS + SAXS revealed information of $LiCoO_2$ particles with physical dimensions from 6.2 μm to 3.7 Å, and the WAXS measured lattice plane spacings of distances from 4.2 Å to 0.9 Å. Therefore, their combination yielded information about corresponding particle size changes and crystal phase evolution.

Figure 2c displays the waterfall plot of the selected WAXS and part of the SAXS range data. The evolution of the $LiCoO_2$ Bragg reflections suggested the dimming of all indicated reflections during over-lithiation. To highlight some of the Bragg peaks, Fig. S3 compares the WAXS data at different statuses. The WAXS data shows no identifiable shifts in the Bragg peaks of $LiCoO_2$, suggesting no lattice expansion and, thus, no intercalation of $LiCoO_2$. Instead, Li^+ reacted with $LiCoO_2$ according to the reactions expressed by equations (1) and (2). The presence of reactions (1) and (2) was also supported by the emergence and growth of Li_2O Bragg peaks accompanying gradually reduced intensities of $LiCoO_2$ peaks. Moreover, Fig. S3 shows that the emerging (220) and (111) peaks of Li_2O were much broader than the Bragg peaks of $LiCoO_2$. The broad peaks indicated the nanocrystalline or highly strained nature of the formed Li_2O, which was expected as this phase emerged within $LiCoO_2$ grains and contributed to the disintegration observed in the USAXS/SAXS. The formation of nano-sized Li_2O particles supported the appearance of the broad peak at around 4×10^{-1}/Å in Figure 2b.

To highlight the change of the USAXS and SAXS data during the discharging process, we normalized the intensity by dividing all scans using the first scan and obtained the relative intensity (RI) plot. Figure 2d can be divided into three regions, (1) a low Q region (10^{-4}/Å to 10^{-3}/Å) that corresponded to large particle sizes (6.3 μm to 0.63 μm), (2) a middle Q region (10^{-3}/Å to 10^{-1}/Å)

that corresponded to medium particle sizes (630 nm to 6.3 nm), and (3) a high Q region (10^{-1}/Å to 10^{0}/Å) that corresponded to small particle sizes (6.3 nm to 0.63 nm). The overall trend shows that the RI value reduced in the low Q region while it increased in the middle and the high Q regions. This trend suggested that large $LiCoO_2$ particles and agglomerates cracked into smaller particles during the over-lithiation process, as shown by the inserted schematic diagram in Figure 2d. In addition, the valley at the low Q region gradually shifted to smaller Q values during the test, indicating that small $LiCoO_2$ particles and agglomerates broke first, and large particles broke at the end of the over-lithiation process. For reference, this trend is clearly shown in Fig. S4, where the blue region, corresponding to the valley in Figure 2d, moved from small to large d-spacing values during the test. The cracking of large $LiCoO_2$ particles and agglomerates generated small particles with a broad size distribution, ranging from 2 nm to 1.5 μm, leading to a broad peak in the middle Q region. Additionally, a sharp peak appeared in the high Q region, and its intensity gradually increased during the test. The physical dimension of the peak was around 1.5 nm, which might be from the formation of nanolayers of differing compositions within the original $LiCoO_2$ particles, forming a core-shell structure, or the particle breakup and generation of nano-particles (Fig. S5) [37].

The combination of USAXS, SAXS, and WAXS data provided a multiscale characterization for the dynamic of the $LiCoO_2$ electrode during the over-lithiation test. This multiscale characterization uncovered the over-lithiation reaction mechanisms. To be more specific, the WAXS data (Fig. S3) suggests the formation of Li_2O crystal with a small particle size as the corresponding WAXS peaks are broad. The result matched well with the appearing feature at around 1.5 nm in the SAXS data (Figure 2b, d). In addition, the WAXS data (Fig. S3, Figure 2c) indicates the reducing amount of $LiCoO_2$ particles as the intensities of the $LiCoO_2$ peaks gradually

reduced during the test. This phenomenon matched with the reduced RI values at micrometer-scale in the USAXS data (Figure 2d), suggesting the reduced number of particles in micrometer sizes. These insights are unattainable in previous studies that detect either micrometer-sized features or nano-sized features [17-21].

Operando Transmission X-ray Microscopy to Study $LiCoO_2$ Over-Lithiation

To visualize the morphological evolution of $LiCoO_2$ particles, TXM was applied to monitor $LiCoO_2$ electrodes during the over-lithiation test. Figure 3a shows the SEM image of $LiCoO_2$ powder before discharge. The powder contains micron-sized secondary particles that are composed of primary particles with 2.1 μm diameter. The cross-section SEM image in Figure 3b shows the morphology of the $LiCoO_2$ particles before discharge. The electrode was prepared extremely thin to eliminate overlapping between $LiCoO_2$ particles for a good TXM image. Figure 3c displays the discharge curve of $LiCoO_2$ during the over-lithiation experiment at a C/2 rate. A specific capacity of 770 mA h/g was obtained when the $LiCoO_2$ was discharged to 0.5 V during TXM measurements, comparable to the specific capacity obtained from the electrode of the synchrotron scattering measurements shown in Figure 2a. The voltage rapidly declined until plateauing at around 1.0 V, with a gradual decline in voltage and beginning of instability at around 320 mA h/g. The voltage fluctuation could be from the breakup of the $LiCoO_2$ particles that introduced unstable contact between the cathode and the anode. This fluctuation should not affect the over-lithiation experiment because the voltage value quickly returned to the plateau at around 1.0 V. SI_video1 shows the evolution of the $LiCoO_2$ electrode morphology during the over-lithiation experiment. Five representative points are selected in Figure 3c, and the corresponding microscopy images are displayed in Figure 3P1-P5. The result indicated that $LiCoO_2$ particles and agglomerates cracked and eventually pulverized during the over-lithiation process. In addition,

particles with larger physical dimensions showed more resistance to the cracking because small particles cracked in the early stage while big particles remained intact and started cracking only at the end of the over-lithiation process.

These observations provided a straightforward validation for interpreting the X-ray scattering results shown in Figure 2d, demonstrating the applicability of the X-ray scattering technique for studying polydisperse battery electrodes. Thus, the combination of the TXM and the USAXS-SAXS-WAXS scattering technique provided an enhanced understanding of the electro-chemo-mechanical behavior of $LiCoO_2$ electrodes during operation. With this knowledge, we could use the operando TXM to visualize the mechanical behavior of battery electrodes during cycling and apply the operando X-ray scattering method to quantitatively investigate the mechanical behavior that is not solvable by the TXM because of its spatial resolution (50 nm).

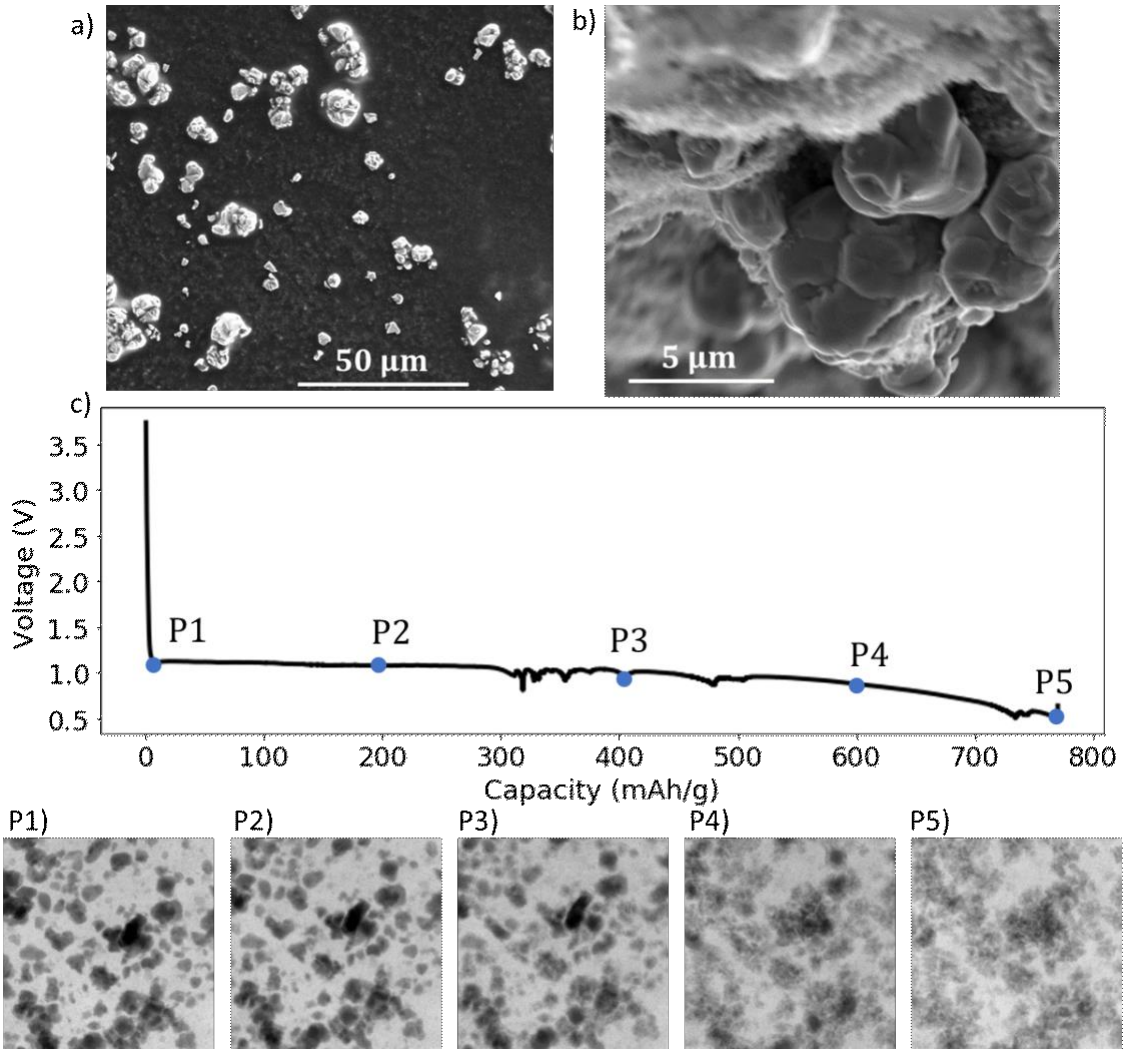

Figure 3. Operando transmission X-ray microscopy (TXM) of a $LiCoO_2$ electrode during over-lithiation to 0.5 V at C/2 rate. (a) SEM image of $LiCoO_2$ active material before discharge, (b) Cross-section SEM image of a $LiCoO_2$ electrode before discharge, (c) Discharge curve during the over-lithiation test. Five points are selected to show their TXM images, as shown in (P1-P5). SI_video1 further shows the evolution of the $LiCoO_2$ electrode during the over-lithiation test.

Investigate $LiCoO_2$ 4.5 V Cycling Stability via Operando Techniques

Surface engineering is an effective method to improve the electrochemical performance of battery electrodes [5]. For example, existing studies show that a PEDOT coating can extend the cycle life of $LiMn_2O_4$ by 70 % [11] and $LiNi_{0.8}Co_{0.1}Mn_{0.1}O_2$ by 500 % [38]. Here, we combined the operando TXM and X-ray scattering techniques to study the electro-chemo-mechanical behavior of $LiCoO_2$ electrodes with a fast cycling rate (5C and 10C) and high upper cutoff voltage (4.5 V). The effect

of the PEDOT coating on the electro-chemo-mechanical behavior of $LiCoO_2$ electrodes was also investigated using the operando synchrotron-based X-ray scattering technique.

Figure 4 displays the evolution of a pristine $LiCoO_2$ electrode undergoing a high rate (10C) and high voltage (4.5 V) cycling measured by the TXM technique. Figure 4a shows that the capacity decreased from 130.7 mA h/g to 37.4 mA h/g after only 30 cycles. The fast capacity degradation was from the high rate and high upper cutoff voltage during the test. Figure 4b shows a 3-by-3 LFOV mosaic of the $LiCoO_2$ electrode. $LiCoO_2$ particles and agglomerates were randomly dispersed with little overlapping because of the relatively low active materials loading (1 mg/cm^2). SI_video2 compares the change of the 3-by-3 LFOV mosaic before and after cycling to illustrate the expansion of primary particles and agglomerates. The two microscopy images were transferred to binary radiograph for quantitative analysis (Fig. S6). Table 1 compares the projected areas of the ten randomly selected particles before and after cycling. The area increased for all ten particles, suggesting the expansion of $LiCoO_2$ primary particles, the cracking of the $LiCoO_2$ secondary particles, and the forming side products on the $LiCoO_2$ surface during cycling. The volume expansion and side product formation could be the reasons for the fast capacity degradation of $LiCoO_2$ electrodes during the 4.5 V high voltage cycling test. The area increased 6.89% on average with a broad distribution, which could be caused by the anisotropic expansion of the $LiCoO_2$. A computed tomography study is needed to accurately describe the volume expansion of $LiCoO_2$ particles, which is not trivial and warrants further investigation.

An operando study was conducted using the HRES mode with 50 nm resolution on the particle 4 labeled in Figure 4b. SI_video3 shows the evolution of the particle during the cycling test. The video suggests that the bulk of the $LiCoO_2$ particle remained intact without noticeable cracks, while the edges of the particle continued changing during the test. Figure 4c compares the first and

last frames of the video representing the particle before and after the cycling test. Noticeable differences could be identified on the edges. To quantitatively analyze the evolution of the particle, we processed and binarized the radiographs. SI_video4 shows a sequence of the binary images for the particle during cycling. The binary images were used to calculate the evolution of the projected area during cycling, as shown in Figure 4d. The projected area kept increasing during cycling with some fluctuation. The fluctuation could be from different state-of-charge (SOC) of the $LiCoO_2$ particles during the measurement. The projected area increased from 39.8 μm^2 to 46.4 μm^2 after the cycling test, indicating side product formation on the $LiCoO_2$ surface or the volume expansion of the $LiCoO_2$ particle.

The operando TXM experiment suggests the following findings on the $LiCoO_2$ mechanical behavior during its 4.5 V high-voltage cycling. Firstly, $LiCoO_2$ primary particles and agglomerates expanded during the cycling test (Table 1, Figure 4d). The expansion could change the contact between the electrode particles and conductive agents, leading to poor rate performance of the electrodes. Secondly, most of the $LiCoO_2$ particles and agglomerates did not break or crack into small pieces due to the relatively small expansion of the particles during cycling (SI_video 2). Thirdly, the edge regions of the $LiCoO_2$ particles changed significantly during cycling (Figure 4c and SI_video 3 and 4). The surface degradation could increase the charge-transfer resistance of the electrode and, thus, introduced kinetic degradation of the LIBs.

Two strategies could be proposed for designing battery materials based on the findings. Firstly, the materials should show slight volume expansion during Li insertion and extraction. For example, $Li_4Ti_5O_{12}$ is a "zero-strain" material that shows negligible volume expansion (0.2%) during cycling, resulting in excellent cycling stability [39]. Secondly, the materials need to be compatible with electrolytes to reduce the side product formation. Tremendous effort has been put

to stabilize the electrode-electrolyte-interface to improve the electrode's cycling stability, including engineering the surface of electrodes, doping the electrodes with transition metals, and developing high-voltage stable electrolytes [40]. Here, we applied the PEDOT coating to engineer the surface of $LiCoO_2$. The effect of the PEDOT coating on the electro-chemo-mechanical behavior of the $LiCoO_2$ electrode was investigated by X-ray scattering techniques (USAXS, SAXS, WAXS) that could provide a wide spatial range from angstroms to micrometers.

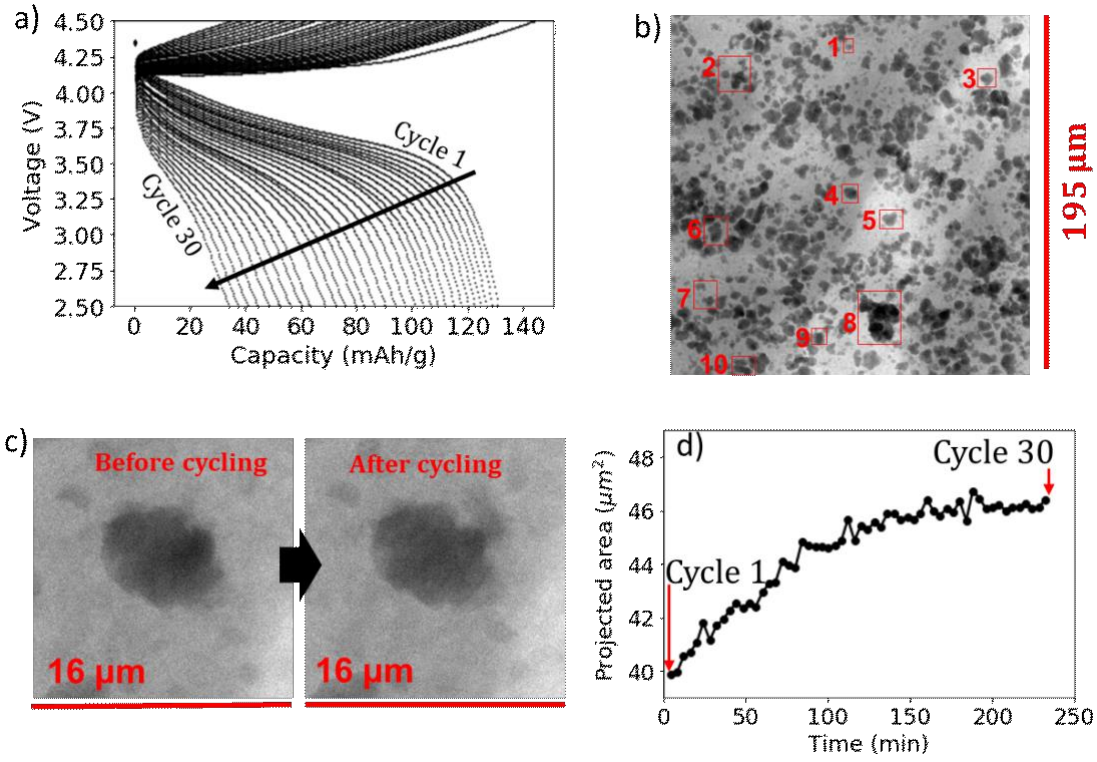

Figure 4. $LiCoO_2$ particle size evolution during 4.5 V high voltage cycling test. (a) The evolution of charge and discharge curves during the cycling test. The voltage range is 2.5 – 4.5 V, and the current is 10C. (b) An LFOV 3-by-3 mosaic of the $LiCoO_2$ electrode. Ten locations are selected for further analysis. (c) HRES nano-CT image of a $LiCoO_2$ particle (particle 4 in b) before and after the cycling test. The evolution of the particle is shown in SI_video 3 and SI_video 4. (d) The evolution of the projected area of the particle during cycling. The gradually increasing projected area indicates the expansion of the primary particle during cycling.

Table 1. The change of the projected area of the ten selected particles and agglomerates in Figure 4b after the high-voltage fast-cycling test.

Particle number	The projected area before cycling (μm^2)	The projected area after cycling (μm^2)	Area change
1	9.32	10.47	12.27%
2	91.26	96.05	5.25%
3	25.79	27.58	6.94%
4	40.84	45.86	12.29%
5	32.09	34.45	7.36%
6	45.89	47.94	4.47%
7	30.45	33.04	8.48%
8	330.27	338.75	2.57%
9	30.67	32.85	7.09%
10	54.29	55.45	2.14%

Operando synchrotron X-ray scattering was applied to study the electro-chemo-mechanical behavior of $LiCoO_2$ during the high voltage cycling test. The technique can capture features of less than 50 nm, the resolution of the TXM technique. Also, the effect of a PEDOT coating on the electro-chemo-mechanical behavior of $LiCoO_2$ electrodes during the cycling test was investigated. As the cycling rate was high (5C), test protocols were carefully designed to allow the measurement to be taken when the electrodes were not cycled. Fig. S7 shows that a 10-min rest step was inserted every five cycles to ensure that at least one measurement was collected at the rest status without SOC variation. Figure 5a compares the capacity degradation of $LiCoO_2$ electrodes with and without the PEDOT coating. The capacity of the pristine $LiCoO_2$ decreased from 154.3 mA h/g to 3.6 mA h/g after 54 cycles. In comparison, the capacity of the PEDOT-coated $LiCoO_2$ decreased from its maximum capacity (146.3 mA h/g at the sixth cycle) to 136.3 mA h/g within the same test time. The PEDOT-coated $LiCoO_2$ only reached 29 cycles due to less capacity fade and, thus, longer average charge and discharge time per cycle. More cycling data of the PEDOT-coated cell can be

found in Fig. S8, collected after the operando X-ray scattering. Thus, the PEDOT coating significantly improved the cycling stability of the $LiCoO_2$ electrode.

The USAXS + SAXS data after different cycles for the two types of cells are shown in Figure 5b, c. The evolution of the USAXS + SAXS data was remarkably different between the two electrodes. At the low Q region (10^{-4} /Å to 2×10^{-4} /Å) that corresponded to large particle sizes (6 μm to 3 μm), the RI value increased for both the pristine $LiCoO_2$ and the PEDOT-coated $LiCoO_2$. The RI value at 10^{-4} /Å after five cycles increased more in the pristine $LiCoO_2$ than in the PEDOT-coated $LiCoO_2$. In addition, the maximum RI value at 10^{-4} /Å was higher in the pristine $LiCoO_2$ electrode than that in the PEDOT-coated $LiCoO_2$. The increased RI value in the low Q region suggested that the number of $LiCoO_2$ particles/agglomerates with the size of 3 μm to 6 μm increased during the cycling test. The increased number of $LiCoO_2$ particles could be from either expanding small $LiCoO_2$ particles or the breakup of large $LiCoO_2$ agglomerates (> 6.2 um). Compared to the pristine $LiCoO_2$, the PEDOT-coated $LiCoO_2$ electrode showed a smaller increase of the RI values, suggesting the PEDOT coating inhibited the volume expansion of $LiCoO_2$ particles or the breakup of large $LiCoO_2$ agglomerates.

The difference of the USAXS + SAXS data in the two $LiCoO_2$ electrodes was more significant in the middle to high Q region (10^{-3} /Å to 10^{-0} /Å), as shown in Figure 5b, c. Three prominent peaks could be identified at around 10^{-2} /Å, 10^{-1} /Å, and 5×10^{-1} /Å, as labeled by dashed lines in the two figures. The corresponding particle/structure sizes were approximately 60 nm, 6 nm, and 1.2 nm. These sizes matched well with $LiCoO_2$ surface deterioration scales (tens of nanometers) [41] and side products from electrolyte decomposition like LiF and $LiCO_3$ (a few nanometers) [42]. The intensities of the peaks gradually increased, and the locations shifted to lower Q regions, indicating that the concentration and the size of the nano-sized features increased during cycling. However,

the peak 1 in the PEDOT-coated $LiCoO_2$ started at a higher Q value (2.5×10^{-2} /Å) than that in the pristine $LiCoO_2$ (1.2×10^{-2} /Å), indicating that the surface layer formed in PEDOT-coated $LiCoO_2$ (25 nm) was thinner than that formed in the pristine $LiCoO_2$ (52 nm) after five cycles.

The PEDOT coating vastly inhibited the formation of the nanoscale features during cycling. Figure 5d, e shows that the peak 1 and 2 in the PEDOT-coated $LiCoO_2$ grew much less in intensity than those in the pristine $LiCoO_2$, indicating that the PEDOT coating inhibited the $LiCoO_2$ surface deterioration and electrolyte decomposition. These results demonstrated that the PEDOT coating alleviated $LiCoO_2$ surface deterioration, reduced the amount of side product from electrolyte decomposition, and inhibited $LiCoO_2$ particles/agglomerates expansion during the 4.5 V high voltage cycling. The mechanisms helped explain the reduced capacity degradation in the PEDOT-coated $LiCoO_2$ (Figure 5a). Thus, inhibiting the formation of these nanoscale features is essential to protect the $LiCoO_2$ from fast degradation during a high-voltage cycling test, and engineering the electrode surface is an effective method to protect the $LiCoO_2$.

By connecting the atomic-scale behavior to bulk structure evolution, the operando techniques provided us a toolbox to correlate the crystal structure evolution with bulk mechanical degradation of battery electrodes. This ability will promote the development of the next-generation LIBs with high energy density and long cycle life. Moving forward, we can apply these techniques for multiscale characterization of other advanced battery electrode materials, such as Ni-rich cathodes and Li-rich cathodes.

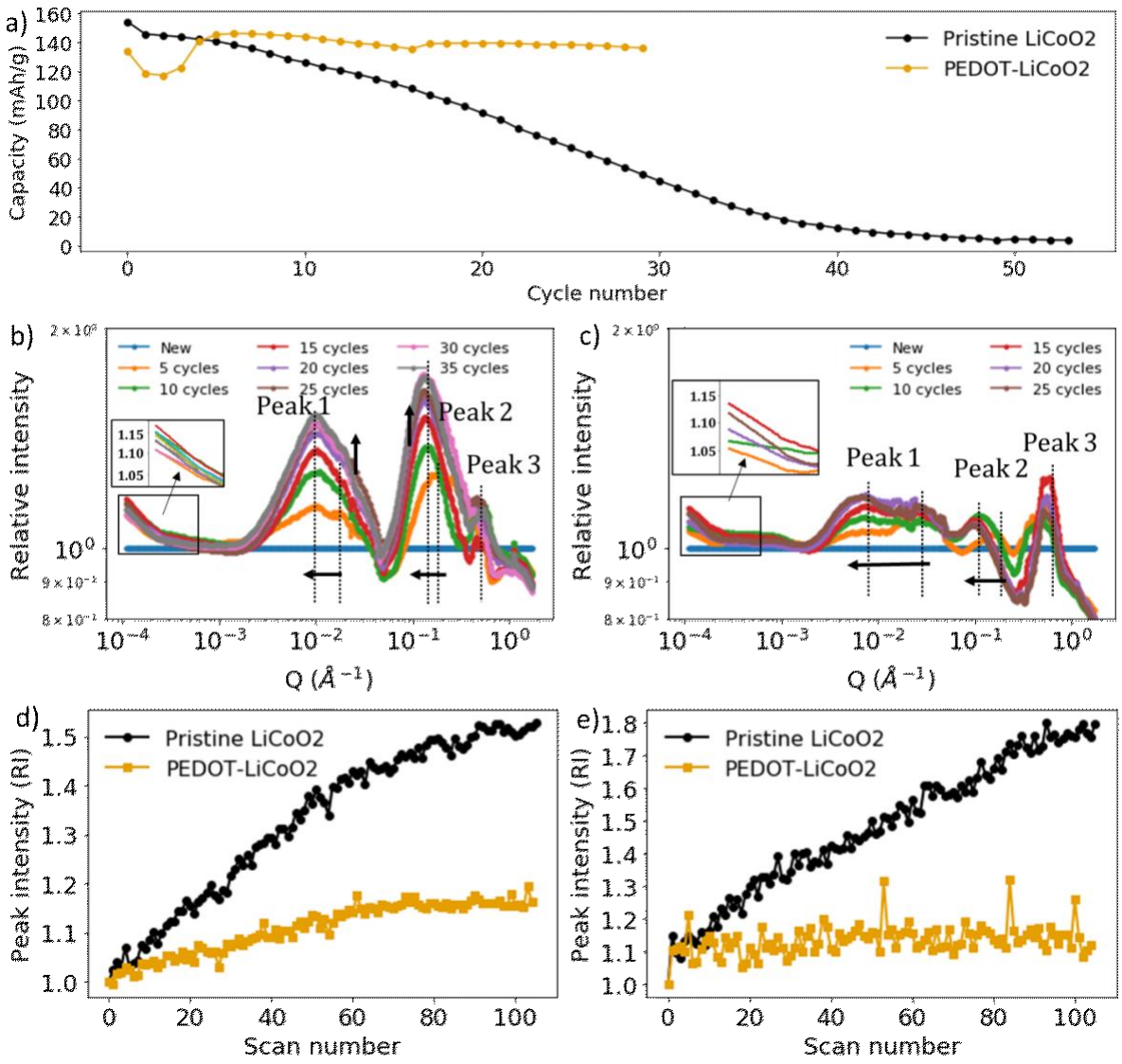

Figure 5. Operando synchrotron X-ray scattering studies $LiCoO_2$ electrodes evolution during 4.5 V high voltage cycling. (a) Discharge capacity evolution during the cycling test at 5C. The total test time is the same for the two cells. Fast capacity fading leads to more cycle numbers for the pristine $LiCoO_2$ electrode. (b) (c) USAXS + SAXS data for pristine $LiCoO_2$ (b) and PEDOT-coated $LiCoO_2$ (c) after different cycles. The inserted figure zooms in the low Q region. (d) (e) The evolution of the relative intensity of peak 1 (d) and peak 2 (e) in figure (b) and (c).

Conclusions

Multimodal operando techniques are developed and applied to investigate the electro-chemo-mechanical behavior of $LiCoO_2$ electrodes. The combination of TXM and synchrotron-based X-ray scattering techniques provides straightforward microscopy images/videos to show the evolution of $LiCoO_2$ particles during cycling and quantitative information on the electrode

particles distribution from angstroms to micrometers. During an over-lithiation experiment from 3.0 V – 0.5 V, $LiCoO_2$ particles crack and eventually pulverize, wherein larger particles show better resistance to the cracking process. During a high voltage cycling test from 3.0 V – 4.5 V, nanometer-scale features form in the $LiCoO_2$ electrode, resulting in fast capacity degradation. We deploy this understanding to demonstrate enhanced stability of $LiCoO_2$ electrodes during high voltage cycling tests by engineering the electrode surface. Moving forward, these multimodal techniques can be used to investigate the electro-chemo-mechanical behavior of other promising battery electrodes for developing advanced LIBs, such as Ni-rich cathodes and Li-rich cathodes.

Acknowledgments

This work was supported by the National Science Foundation (NSF) CAREER Award (CMMI1751605), Scott Institute Seed Grants, and INCUBATE seed funding from Carnegie Mellon University. N. Nakamura is supported by a National Defense Science and Engineering Graduate (NDSEG) Fellowship. P. Choi is supported by the National Science Foundation under Grant No. CBET-1705321.This research used 9-ID-C beamline and other resources in Advanced Photon Source, Argonne National Laboratory under Contract No. DE-AC02-06CH11357. The authors thank Prof. Jay F Whitacre in CMU for sharing their equipment and lab facilities.

Author Contributions Statement

Laisuo Su: Conceptualization, Data curation, Formal analysis; Writing - original draft, Paul Choi: Data curation, Formal analysis, Writing – original draft, Nathan Nakamura: Data curation, Formal analysis, Harry Charalambous: Data curation, Shawn Litster: Resources, Writing - review & editing, Jan Ilavsky: Resources, Formal analysis, B. Reeja-Jayan: Conceptualization, Resources, Writing - review & editing.

References

1. Y. Ding, D. Mu, B. Wu, R. Wang, Z. Zhao, F. Wu. Recent Progresses on Nickel-Rich Layered Oxide Positive Electrode Materials Used in Lithium-Ion Batteries for Electric Vehicles. Appl Energ, 195 (2017),586-599
2. R. Koerver, W. Zhang, L. de Biasi, S. Schweidler, A. O. Kondrakov, S. Kolling, et al. Chemo-Mechanical Expansion of Lithium Electrode Materials – On the Route to Mechanically Optimized All-Solid-State Batteries. Energ Environ Sci, 11 (2018),2142-2158
3. P. R. Shearing. Batteries: Imaging Degradation. Nat Energy, 1 (2016),1-2
4. M. Ebner, F. Marone, M. Stampanoni, V. Wood. Visualization and Quantification of Electrochemical and Mechanical Degradation in Li Ion Batteries. Science, 342 (2013),716-720
5. Y. Li, X. Cheng, Y. Zhang, K. Zhao. Recent Advance in Understanding the Electro-Chemo-Mechanical Behavior of Lithium-Ion Batteries by Electron Microscopy. Materials Today Nano, 7 (2019),100040
6. J. Zhu, X. Zhang, H. Luo, E. Sahraei. Investigation of the Deformation Mechanisms of Lithium-Ion Battery Components Using in-Situ Micro Tests. Appl Energ, 224 (2018),251-266
7. S. K. Jha, H. Charalambous, J. S. Okasinski, T. Tsakalakos. Using in Operando Diffraction to Relate Lattice Strain with Degradation Mechanism in a NMC Battery. J Mater Sci, 54 (2019),2358-2370
8. Q. Liu, X. Su, D. Lei, Y. Qin, J. Wen, F. Guo, et al. Approaching the Capacity Limit of Lithium Cobalt Oxide in Lithium Ion Batteries Via Lanthanum and Aluminium Doping. Nat Energy, 3 (2018),936-943
9. A. Mukhopadhyay, B. W. Sheldon. Deformation and Stress in Electrode Materials for Li-Ion Batteries. Prog Mater Sci, 63 (2014),58-116
10. H. Li, H. Zhou. Enhancing the Performances of Li-Ion Batteries by Carbon-Coating: Present and Future. Chem Commun, 48 (2012),1201-1217
11. L. Su, P. M. Smith, P. Anand, B. Reeja-Jayan. Surface Engineering of a LiMn2O4 Electrode Using Nanoscale Polymer Thin Films Via Chemical Vapor Deposition Polymerization. ACS Appl Mater Inter, 10 (2018),27063-27073
12. L. Su, S. K. Jha, X. L. Phuah, J. Xu, N. Nakamura, H. Wang, et al. Engineering Lithium-Ion Battery Cathodes for High-Voltage Applications Using Electromagnetic Excitation. J Mater Sci, 55 (2020),12177-12190
13. X. Ke, Z. Zhao, J. Liu, Z. Shi, Y. Li, L. Zhang, et al. Improvement in Capacity Retention of Cathode Material for High Power Density Lithium Ion Batteries: The Route of Surface Coating. Appl Energ, 194 (2017),540-548
14. J. Lu, Q. Peng, W. Wang, C. Nan, L. Li, Y. Li. Nanoscale Coating of LiMO2 (M= Ni, Co, Mn) Nanobelts with Li+-Conductive Li2TiO3: Toward Better Rate Capabilities for Li-Ion Batteries. J Am Chem Soc, 135 (2013),1649-1652
15. J. Wang, H. Luo, Y. Liu, Y. He, F. Fan, Z. Zhang, et al. Tuning the Outward to Inward Swelling in Lithiated Silicon Nanotubes Via Surface Oxide Coating. Nano Lett, 16 (2016),5815-5822
16. P. Yan, J. Zheng, J. Liu, B. Wang, X. Cheng, Y. Zhang, et al. Tailoring Grain Boundary Structures and Chemistry of Ni-Rich Layered Cathodes for Enhanced Cycle Stability of Lithium-Ion Batteries. Nat Energy, 3 (2018),600-605

17. C. Choe, W. Jung, J. Byeon. Damage Evaluation in Lithium Cobalt Oxide/Carbon Electrodes of Secondary Battery by Acoustic Emission Monitoring. Mater Trans, 56 (2015),269-273
18. J. Wu, S. Yang, W. Cai, Z. Bi, G. Shang, J. Yao. Multi-Characterization of LiCoO2 Cathode Films Using Advanced AFM-Based Techniques with High Resolution. Sci Rep-Uk, 7 (2017)
19. J. Ma, Y. Liu, P. Hao, J. Wang, Y. Zhang. Effect of Different Oxide Thickness on the Bending Young's Modulus of SiO2@Sic Nanowires. Sci Rep-Uk, 6 (2016)
20. A. Kushima, J. Y. Huang, J. Li. Quantitative Fracture Strength and Plasticity Measurements of Lithiated Silicon Nanowires by in Situ TEM Tensile Experiments. ACS Nano, 6 (2012),9425-9432
21. M. G. Boebinger, O. Yarema, M. Yarema, K. A. Unocic, R. R. Unocic, V. Wood, et al. Spontaneous and Reversible Hollowing of Alloy Anode Nanocrystals for Stable Battery Cycling. Nat Nanotechnol,(2020)
22. C. L. Berhaut, D. Z. Dominguez, D. Tomasi, C. Vincens, C. Haon, Y. Reynier, et al. Prelithiation of Silicon/Graphite Composite Anodes: Benefits and Mechanisms for Long-Lasting Li-Ion Batteries. Energy Storage Materials, 29 (2020),190-197
23. C. L. Berhaut, D. Z. Dominguez, P. Kumar, P. Jouneau, W. Porcher, D. Aradilla, et al. Multiscale Multiphase Lithiation and Delithiation Mechanisms in a Composite Electrode Unraveled by Simultaneous Operando Small-Angle and Wide-Angle X-Ray Scattering. Acs Nano, 13 (2019),11538-11551
24. N. Yang, Y. Song, R. Liu. In-Situ Transmission X-Ray Microscopy Probed by Synchrotron Radiation for Li-Ion Batteries. Frontiers in Energy Research, 6 (2018),56
25. Y. Lyu, X. Wu, K. Wang, Z. Feng, T. Cheng, Y. Liu, et al. An Overview on the Advances of LiCoO2 Cathodes for Lithium‐Ion Batteries. Adv Energy Mater, 11 (2021), 2000982
26. Y. Jiang, C. Qin, P. Yan, M. Sui. Origins of Capacity and Voltage Fading of LiCoO2 upon High Voltage Cycling. J Mater Chem a, 7 (2019), 20824-20831
27. J. Nelson Weker, A. M. Wise, K. Lim, B. Shyam, M. F. Toney. Operando Spectroscopic Microscopy of LiCoO2 Cathodes Outside Standard Operating Potentials. Electrochim Acta, 247 (2017),977-982
28. Y. Xu, E. Hu, K. Zhang, X. Wang, V. Borzenets, Z. Sun, et al. In Situ Visualization of State-of-Charge Heterogeneity within a LiCoO2 Particle that Evolves upon Cycling at Different Rates. Acs Energy Lett, 2 (2017),1240-1245
29. L. Su, J. L. Weaver, M. Groenenboom, N. Nakamura, E. Rus, P. Anand, et al. Tailoring Electrode–Electrolyte Interfaces in Lithium-Ion Batteries Using Molecularly Engineered Functional Polymers. ACS Appl Mater Inter,(2021)
30. J. Ilavsky, F. Zhang, R. N. Andrews, I. Kuzmenko, P. R. Jemian, L. E. Levine, et al. Development of Combined Microstructure and Structure Characterization Facility for in Situ and Operando Studies at the Advanced Photon Source. J Appl Crystallogr, 51 (2018),867-882
31. J. Ilavsky, P. R. Jemian, A. J. Allen, F. Zhang, L. E. Levine, G. G. Long. Ultra-Small-Angle X-Ray Scattering at the Advanced Photon Source. J Appl Crystallogr, 42 (2009),469-479
32. S. Frisco, A. Kumar, J. F. Whitacre, S. Litster. Understanding Li-Ion Battery Anode Degradation and Pore Morphological Changes through Nano-Resolution X-Ray Computed Tomography. J Electrochem Soc, 163 (2016),A2636

33. P. M. Smith, L. Su, W. Gong, N. Nakamura, B. Reeja-Jayan, S. Shen. Thermal Conductivity of Poly(3,4-Ethylenedioxythiophene) Films Engineered by Oxidative Chemical Vapor Deposition (oCVD). RSC Adv, 8 (2018),19348-19352
34. A. Buades, B. Coll, J. Morel, "A Non-Local Algorithm for Image Denoising,", (IEEE, 2005), pp. 60-65.
35. J. Shu, M. Shui, F. Huang, Y. Ren, Q. Wang, D. Xu, et al. A New Look at Lithium Cobalt Oxide in a Broad Voltage Range for Lithium-Ion Batteries. The Journal of Physical Chemistry C, 114 (2010),3323-3328
36. H. You, C. A. Melendres, Z. Nagy, V. A. Maroni, W. Yun, R. M. Yonco. X-Ray-Reflectivity Study of the Copper-Water Interface in a Transmission Geometry Under in Situ Electrochemical Control. Physical review. B, Condensed matter, 45 (1992),11288
37. Y. Ren, X. Zuo. Synchrotron X-Ray and Neutron Diffraction, Total Scattering, and Small-Angle Scattering Techniques for Rechargeable Battery Research. Small Methods, 2 (2018),1800064
38. G. Xu, Q. Liu, K. K. S. Lau, Y. Liu, X. Liu, H. Gao, et al. Building Ultraconformal Protective Layers on Both Secondary and Primary Particles of Layered Lithium Transition Metal Oxide Cathodes. Nat Energy,(2019)
39. C. P. Sandhya, B. John, C. Gouri. Lithium Titanate as Anode Material for Lithium-Ion Cells: A Review. Ionics, 20 (2014),601-620
40. L. Wang, B. Chen, J. Ma, G. Cui, L. Chen. Reviving Lithium Cobalt Oxide-Based Lithium Secondary Batteries-Toward a Higher Energy Density. Chem Soc Rev, 47 (2018),6505-6602
41. Y. Jiang, C. Qin, P. Yan, M. Sui. Origins of Capacity and Voltage Fading of LiCoO2 upon High Voltage Cycling. J Mater Chem A, 7 (2019),20824-20831
42. K. Edström, T. Gustafsson, J. O. Thomas. The Cathode–Electrolyte Interface in the Li-Ion Battery. Electrochim Acta, 50 (2004),397-403